V European Conference on Computational Fluid Dynamics
ECCOMAS CFD 2010
J. C. F. Pereira and A. Sequeira (Eds)
Lisbon, Portugal,14-17 June 2010

THREE-DIMENSIONAL INERTIAL THIN FILM FLOW ON PLANAR SUBSTRATES CONTAINING OCCLUSIONS

Sergii Veremieiev*, Harvey M. Thompson*, Yeaw Chu Lee* and Philip H. Gaskell*

*School of Mechanical Engineering, The University of Leeds,
Leeds, United Kingdom, LS2 9JT
e-mail: s.veremieiev@leeds.ac.uk

Key words: Coating, Thin film flows, Microfluidics, Topography

Abstract. *The effect of inertia on gravity-driven thin film free-surface flow over substrates containing occlusions is considered. Flow is modelled using a depth-averaged form of the governing Navier-Stokes equations, that enables the exact form of the no-slip condition to be applied at occlusion surfaces, and the discrete analogue of the coupled equations solved accurately using an efficient full approximation storage (FAS) algorithm and a full multigrid (FMG) technique. The effects of inertia and occlusion geometry on the resultant free-surface disturbances are illustrated by a series of results for flow past rectangular occlusions which demonstrate how increasing the Reynolds number and/or the occlusion aspect ratio can significantly enhance both the film thickness on the upstream occlusion boundary and the degree of film thinning at its downstream side. The effect of static contact angle on free-surface disturbances induced by rectangular occlusions is also investigated and the results obtained for inertial flow found to be consistent with recent results for Stokes flow.*

1 INTRODUCTION

The deposition of thin film coatings over substrates containing regions of micro-scale topography forms an important component of many natural and scientific processes[1], in substrate cooling and heat transfer applications[2,3], and several precision manufacturing techniques. Examples of the latter can be found in the production of anti-reflective coatings[4], flexible electronic components[5], and in displays and sensors[6], where thin liquid films flow over a distribution of functional topographical features such as light-emitting species on a screen. In industrial coating applications product functionality often depends critically on the coated film thickness distribution and this has stimulated much interest in recent years on understanding the flow mechanisms controlling free-surface disturbances induced by topographic features.

This paper focusses on the particular case of thin film flow past occlusions whose height is significantly larger than the local film thickness. Such flows are found, for example, during pesticide flow over hairy leaf surfaces[7] and within an aerospace bearing chamber where the film flow interacts with chamber supports and nuts. For the latter example, detailed knowledge of the free-surface profile and volume flux within the chamber is essential for optimal design[2]. The present lack of reliable data is testament to the difficulties of studying such systems experimentally, so numerical simulations are likely to be the most viable option in the foreseeable future. Previous numerical studies of three-dimensional, thin film flow past occlusions have been restricted to cases of Stokes flow using either lubrication theory[8] or the Boundary Integral Equation method[2,9].

Flow inertia can also have a significant influence on both the magnitude[10] and stability[11] of free-surface disturbances induced by topography. The present study is the first to consider the additional influence of inertia on three-dimensional free-surface disturbances induced by thin film flow past occlusions. The approach adopted involves the efficient solution of a depth-averaged form of the governing Navier-Stokes equations[10]. Section 2 formulates the flow problems of interest while Section 3 outlines the numerical solution method adopted. Results are presented in Section 4 for the influence of inertia on free-surface disturbances induced by flow past a series of rectangular occlusions. Conclusions are drawn in Section 5.

2 PROBLEM FORMULATION

The problems of interest, shown schematically in Figure 1, are of gravity-driven film flow down a planar surface containing a rectangular occlusion of length L_T ($\ll L_P$) and width W_T ($\ll W_P$), where L_P and W_P are the length and width of the problem domain respectively. The liquid is assumed to be Newtonian and incompressible, with constant viscosity, μ, density, ρ, and surface tension σ. The chosen Cartesian streamwise, X, spanwise, Y, and normal, Z, coordinates are as indicated and the solution domain is bounded from below by the inclined surface $Z = 0$ and from above by the free-surface $Z = H(X, Y, T)$, where $H(X, Y, T)$ is the film thickness at any point in the (X, Y) and at

any time T. The resulting laminar flow is described by the Navier-Stokes and continuity equations, namely:

$$\rho\left(\frac{\partial \boldsymbol{U}}{\partial T}+\boldsymbol{U}\cdot\nabla\boldsymbol{U}\right)=-\nabla P+\nabla\cdot\boldsymbol{T}+\rho\boldsymbol{G}, \tag{1}$$

$$\nabla\cdot\boldsymbol{U}=0, \tag{2}$$

where $\boldsymbol{U}=(U,V,W)$ and P are the fluid velocity and pressure, respectively; $\boldsymbol{T}=\mu\left(\nabla\boldsymbol{U}+(\nabla\boldsymbol{U})^{T}\right)$ is the viscous stress tensor and $\boldsymbol{G}=g_0\left(\sin\theta,0,-\cos\theta\right)$ is the acceleration due to gravity where g_0 is the standard gravity constant.

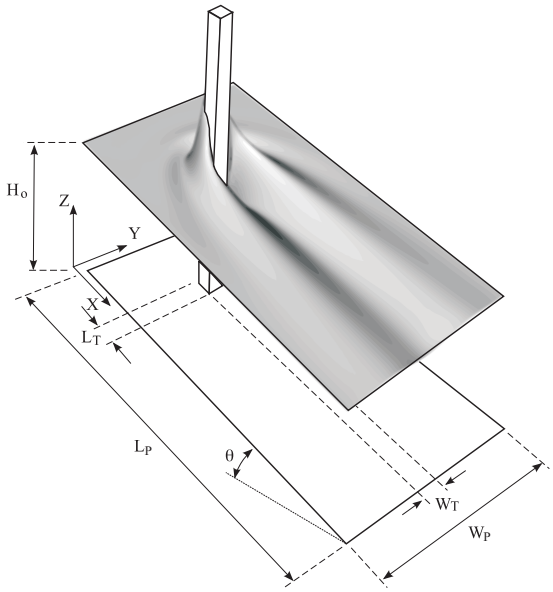

Figure 1: Schematic of gravity-driven film flow past an occlusion.

Taking the reference length-scale in all directions to be the asymptotic, or fully developed, film thickness, H_0, and scaling the velocities by the free-surface (maximum) velocity, $U_0=\rho g_0 H_0^2\sin\theta/2\mu$ apropos the classic Nusselt solution[11], pressure (stress tensor) by $P_0=\mu U_0/H_0$, and time by $T_0=H_0/U_0$, equations (1) and (2) can be rewritten in non-dimensional form as:

$$\mathrm{Re}\left(\frac{\partial \boldsymbol{u}}{\partial t}+\boldsymbol{u}\cdot\nabla\boldsymbol{u}\right)=-\nabla p+\nabla\cdot\boldsymbol{\tau}+\mathrm{St}\boldsymbol{g}, \tag{3}$$

$$\nabla\cdot\boldsymbol{u}=0, \tag{4}$$

where $\boldsymbol{u}=(u,v,w)$, $\boldsymbol{\tau}$ and $\boldsymbol{g}=\boldsymbol{G}/g_0$ are the dimensionless velocity, viscous stress tensor and gravity component, respectively; $\mathrm{Re}=\rho U_0 H_0/\mu$ is the Reynolds number and $\mathrm{St}=2/\sin\theta$ the Stokes number.

The problem is closed by imposing the required no-slip, inflow, outflow, kinematic, free-surface normal and tangential stress boundary conditions, namely:

$$\boldsymbol{u}|_{z=0} = 0, \tag{5}$$

$$\boldsymbol{u}|_{x=0,l_p;y=0,w_p} = \left(z\left(2-z\right),0,0\right), \tag{6}$$

$$\frac{\partial h}{\partial t} + u|_{z=h}\frac{\partial h}{\partial x} + v|_{z=h}\frac{\partial h}{\partial y} - w|_{z=h} = 0, \tag{7}$$

$$-p + \left(\boldsymbol{\tau}|_{z=h}\cdot\boldsymbol{n_h}\right)\cdot\boldsymbol{n_h} = \frac{\kappa}{\mathrm{Ca}}, \tag{8}$$

$$\left(\boldsymbol{\tau}|_{z=h}\cdot\boldsymbol{n_h}\right)\cdot\boldsymbol{t_h} = 0, \tag{9}$$

where $\mathrm{Ca} = \mu U_0/\sigma$ is the capillary number, x, y, z, l_p, w_p, h correspond to their dimensional counterparts, $\boldsymbol{n_h} = \left(-\frac{\partial h}{\partial x}, -\frac{\partial h}{\partial y}, 1\right)\cdot\left[\left(\frac{\partial h}{\partial x}\right)^2 + \left(\frac{\partial h}{\partial y}\right)^2 + 1\right]^{-1/2}$ is the unit normal vector pointing outward from the free surface, $\boldsymbol{t_h}$ is the unit vector tangential to the free surface and $\kappa = -\nabla\cdot\boldsymbol{n_h}$ is the free-surface curvature.

The liquid meets the occlusion at a static contact line with a resulting static contact angle, θ_S, formed at the free-surface in a plane normal to the occlusion boundary. This condition together with a no-slip boundary condition at the boundary of the occlusion Γ are imposed via[8]

$$\nabla h|_{(x,y)\in\Gamma}\cdot\boldsymbol{n_\Gamma} = \tan\left(\theta_S - \frac{\pi}{2}\right), \tag{10}$$

$$\boldsymbol{u}|_{(x,y,z)\in\Gamma} = 0, \tag{11}$$

where $\boldsymbol{n_\Gamma}$ is the outward pointing normal to the occlusion.

2.1 Mathematical formulation

Since the mathematical details are described in detail elsewhere[10], only a very brief overview is provided. A process of depth-averaging is used by adopting a long-wave approximation that $\varepsilon = H_0/L_0 \ll 1$, where $L_0 = H_0/\left(6\mathrm{Ca}\right)^{1/3}$ is the characteristic in-plane capillary length scale. The required friction and dissipation terms[10] are obtained by assuming the self-similar velocity profiles:

$$u = 3\bar{u}\left(\xi - 1/2\xi^2\right), \quad v = 3\bar{v}\left(\xi - 1/2\xi^2\right), \tag{12}$$

where $\xi = z/h$. Then the depth-averaged form (DAF) of the momentum equations (3) and the continuity equation (4) for the unknown averaged velocities $\bar{u}\left(x,y,t\right) = \frac{1}{h}\int_0^h u\,dz$, $\bar{v}\left(x,y,t\right) = \frac{1}{h}\int_0^h v\,dz$ and the film thickness $h\left(x,y,t\right)$ respectively are:

$$\varepsilon\mathrm{Re}\left[\frac{\partial\bar{u}}{\partial t} - \frac{u}{5h}\frac{\partial h}{\partial t} + \frac{6}{5}\left(\bar{u}\frac{\partial\bar{u}}{\partial x} + \bar{v}\frac{\partial\bar{u}}{\partial y}\right)\right] = \frac{\partial}{\partial x}\left[\frac{\varepsilon^3}{\mathrm{Ca}}\nabla^2 h - 2\varepsilon h\cot\theta\right] - \frac{3\bar{u}}{h^2} + 2, \tag{13}$$

$$\varepsilon \mathrm{Re}\left[\frac{\partial \bar{v}}{\partial t}-\frac{u}{5h}\frac{\partial h}{\partial t}+\frac{6}{5}\left(\bar{u}\frac{\partial \bar{v}}{\partial x}+\bar{v}\frac{\partial \bar{v}}{\partial y}\right)\right]=\frac{\partial}{\partial y}\left[\frac{\varepsilon^3}{\mathrm{Ca}}\nabla^2 h-2\varepsilon h\cot\theta\right]-\frac{3\bar{v}}{h^2}, \tag{14}$$

$$\frac{\partial \bar{h}}{\partial t}+\frac{\partial}{\partial x}\left(h\bar{u}\right)+\frac{\partial}{\partial y}\left(h\bar{v}\right)=0. \tag{15}$$

Problems are closed using averaged forms for the outflow/inflow conditions and the assumption of fully developed flow both upstream and downstream, namely:

$$\bar{u}|_{x=0}=2/3,\quad \bar{v}|_{x=0}=\frac{\partial \bar{u}}{\partial x}|_{x=l_p}=\frac{\partial \bar{v}}{\partial x}|_{x=l_p}=\frac{\partial \bar{u}}{\partial y}|_{y=0,w_p}=\frac{\partial \bar{v}}{\partial y}|_{y=0,w_p}=0, \tag{16}$$

$$h|_{x=0}=1,\quad \frac{\partial h}{\partial x}|_{x=l_p}=\frac{\partial h}{\partial y}|_{y=0,w_p}=0. \tag{17}$$

In addition the static contact line and no-slip conditions take the form:

$$\varepsilon\nabla h|_{(x,y)\in\Gamma}\cdot\boldsymbol{n}_{\boldsymbol{\Gamma}}=\tan\left(\theta_S-\frac{\pi}{2}\right),\quad \bar{u}|_{(x,y)\in\Gamma}=\bar{v}|_{(x,y)\in\Gamma}=0. \tag{18}$$

3 METHOD OF SOLUTION

The method of solution is based on that described in detail recently[10], so only a brief outline is given below.

3.1 Spatial Discretisation

Equations (13) to (15), incorporating appropriate friction and dispersion terms, are solved subject to the applicable boundary conditions on a rectangular computational domain, $(x,y)\in\Omega=(0,l_p)\times(0,w_p)$, subdivided using a regular spatially staggered mesh arrangement of cells having sides of length Δx and width Δy. The unknown variables, film thickness, h, and the velocity components, $\bar{u}$, $\bar{v}$, are located at cell centres, (i,j), and cell faces, $(i+1/2,j)$, $(i,j+1/2)$, respectively. Solving the momentum equations (13) and (14) at cell faces with the convection and time derivative terms grouped together to simplify their numerical treatment, and omitting for the sake of convenience the overbar denoting velocity averaging, results in the following second-order accurate in space discretisation scheme:

$$\varepsilon \mathrm{Re}\left(\frac{\partial u}{\partial t}-\frac{u}{5h}\frac{\partial h}{\partial t}+\frac{6}{5}F\left[u\right]\right)_{i+1/2,j}$$

$$-\frac{\varepsilon^3}{\mathrm{Ca}}\left(\frac{h_{i+1,j+1}-2h_{i+1,j}+h_{i+1,j-1}-h_{i,j+1}+2h_{i,j}-h_{i,j-1}}{\Delta x\Delta y^2}\right.$$

$$\left.+\frac{h_{i+2,j}-3h_{i+1,j}+3h_{i,j}-h_{i-1,j}}{\Delta x^3}\right)+2\varepsilon\cot\theta\frac{h_{i+1,j}-h_{i,j}}{\Delta x}+\frac{3u_{i+1/2,j}}{h^2_{i+1/2,j}}-2=0, \tag{19}$$

$$\varepsilon \mathrm{Re}\left(\frac{\partial v}{\partial t}-\frac{v}{5h}\frac{\partial h}{\partial t}+\frac{6}{5}F\left[v\right]\right)_{i,j+1/2}$$

$$-\frac{\varepsilon^3}{\mathrm{Ca}}\left(\frac{h_{i+1,j+1}-2h_{i,j+1}+h_{i-1,j+1}-h_{i+1,j}+2h_{i,j}-h_{i-1,j}}{\Delta x^2\Delta y}\right.$$
$$\left.+\frac{h_{i,j+2}-3h_{i,j+1}+3h_{i,j}-h_{i,j-1}}{\Delta y^3}\right)+2\varepsilon\cot\theta\frac{h_{i,j+1}-h_{i,j}}{\Delta y}+\frac{3v_{i,j+1/2}}{h_{i,j+1/2}^2}=0, \qquad (20)$$

$$\frac{\partial h_{i,j}}{\partial t}+\frac{h_{i+1/2,j}u_{i+1/2,j}-h_{i-1/2,j}u_{i-1/2,j}}{\Delta x}+\frac{h_{i,j+1/2}v_{i,j+1/2}-h_{i,j-1/2}v_{i,j-1/2}}{\Delta y}=0, \qquad (21)$$

where $F[\omega]=u\frac{\partial\omega}{\partial x}+v\frac{\partial\omega}{\partial y}$ is the convective operator and the following terms are interpolated from neighbouring nodes: $h_{i\pm1/2,j}=(h_{i\pm1,j}+h_{i,j})/2$, $h_{i,j\pm1/2}=(h_{i,j\pm1}+h_{i,j})/2$. The convective operator $F[\omega]$ is discretized using a second-order accurate total variation diminishing (TVD) scheme[12].

3.2 Temporal Discretisation

The associated time discretisation includes the use of an explicit and second-order accurate in time predictor and a semi-implicit β-method[10] solution stages. For $\beta=1/2$ the method reduces to the second order accurate in time, but conditionally stable Crank-Nicolson scheme, whereas $\beta=1$ leads to the fully implicit first order accurate in time unconditionally stable Laasonen method. The automatic adaptive time-stepping procedure adopted employs an estimate of the local truncation error (LTE) obtained from the difference between an explicit predictor stage and the current solution stage to optimise the size of time steps and thus minimise computational waste.

3.3 Multigrid Solver

The discretized equations are solved using a multigrid strategy with a combined Full Approximation Storage (FAS) and full multigrid (FMG) technique, where errors on a particular computational grid are reduced by employing a hierarchy of successively finer grids, $G^0,\ldots,G^k,\ldots,G^K$, where G^0 denotes the coarsest and G^K the finest grid level. The FMG solution process consists of performing a fixed number of FAS V-cycles on intermediate grid levels $G^k\in[G^1,...,G^{k-1}]$ (usually 1-3 V cycles) and up to 10 V cycles on the finest grid level G^K. Due to the staggered nature of the discretization involved, the relaxation methodology adopted employs a lexicographic box smoothing Gauss-Seidel scheme. Dirichlet boundary conditions are assigned as exact values at the boundary points, whereas Neumann boundary conditions are implemented by employing ghost nodes at the edge of the computational domain.

4 RESULTS

Results are provided which briefly explore the effect of Reynolds number on the resultant free surface disturbance for gravity-driven thin film flow over an inclined substrate with $\theta=\frac{\pi}{6}$ past a rectangular occlusion of aspect ratio $A=W_T/L_T$. For the cases considered $\varepsilon=0.1$, which results in $\mathrm{Ca}=\varepsilon^3/6=0.000167$, and the two-dimensional flow

domain has $l_p = w_p = 80$ and the occlusion is centred at $(x_t, y_t) = (30, 40)$. The multigrid algorithm employs a coarsest grid level G^0 with $n_x^0 = n_y^0 = 64$ and a finest grid level G^4 with $n_x^4 = n_y^4 = 1024$ uniformly spaced cells. At each time step sufficient multigrid V-cycles are performed to reduce residuals on the finest mesh level to below 10^{-6}.

Figure 2 investigates the effect of contact angle θ_S on the three-dimensional free-surface disturbance caused by a square ($A = 1$) occlusion for $\mathrm{Re} = 5$. Increasing the static contact angle θ_S leads to a reduction in film thickness near the upstream boundary and an increase in film thickness at the downstream boundary. These findings are consistent with recent results[2] for $\mathrm{Re} = 0$, however in the first case the free-surface profiles near the occlusion are much more sensitive to the prescribed θ_S owing to the long, thin nature of the occlusions considered in this work.

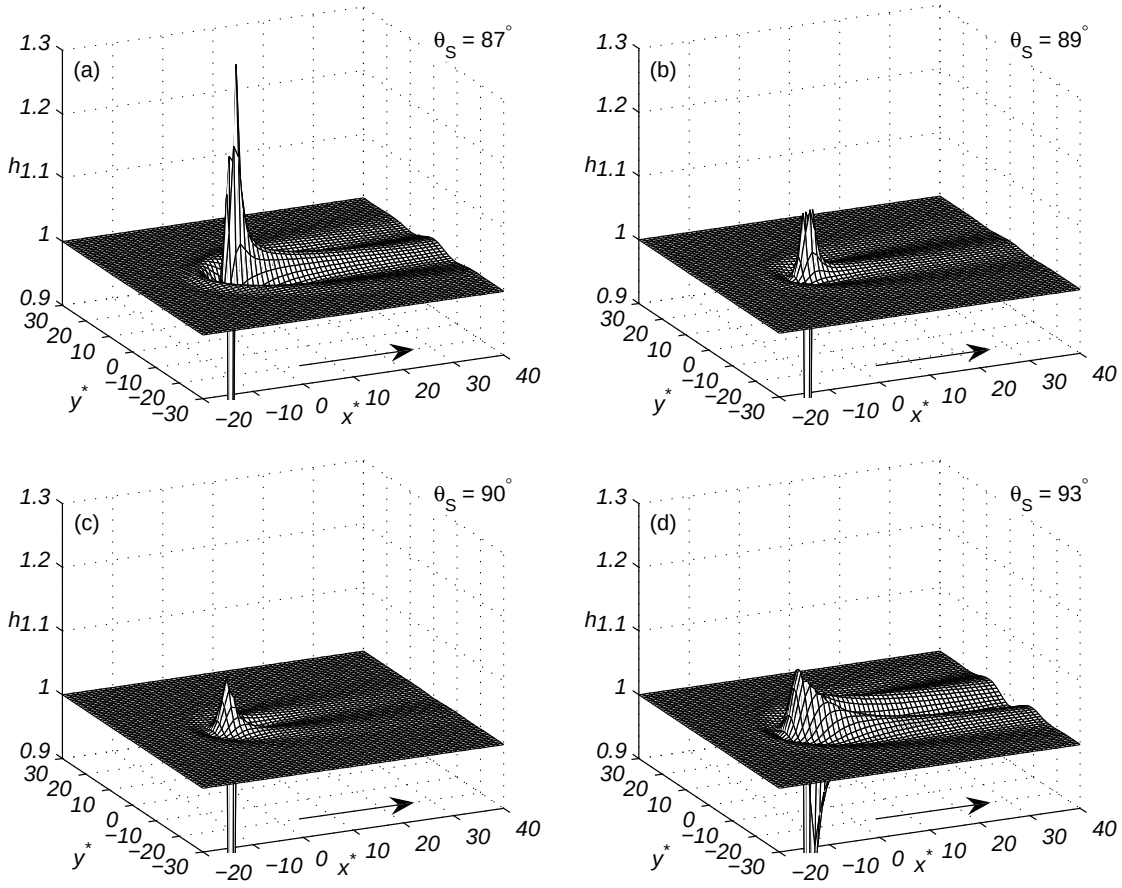

Figure 2: Free-surface plot for flow over a two-dimensional localised square occlusion with $\mathrm{Re} = 5$ showing the effect of contact angle, θ_S, on the free surface disturbance.

The effects of both contact angle θ_S and Reynolds number Re on the streamwise and spanwise centre-line free-surface profiles are described on Figure 3. For a fixed contact angle increasing Re promotes localised film thickening and film thinning at the upstream

and downstream occlusion boundaries respectively. For example, the streamwise profiles in Figure 3 show that increasing Re from 5 to 50 leads to an increase in the film thickness upstream of the occlusion from 1.37 to 1.49 and 0.81 to 0.92 for $\theta_S = 87°$ and 93° respectively. Downstream of the occlusion the effect of increasing Re is to reduce the film thickness. For $\theta_S = 87°$ increasing Re from 5 to 50 leads to film thinning, where the film thickness reduces from 1.40 to 1.36, whereas for $\theta_S = 93°$ this leads to reductions in the film thickness from 0.54 to 0.49.

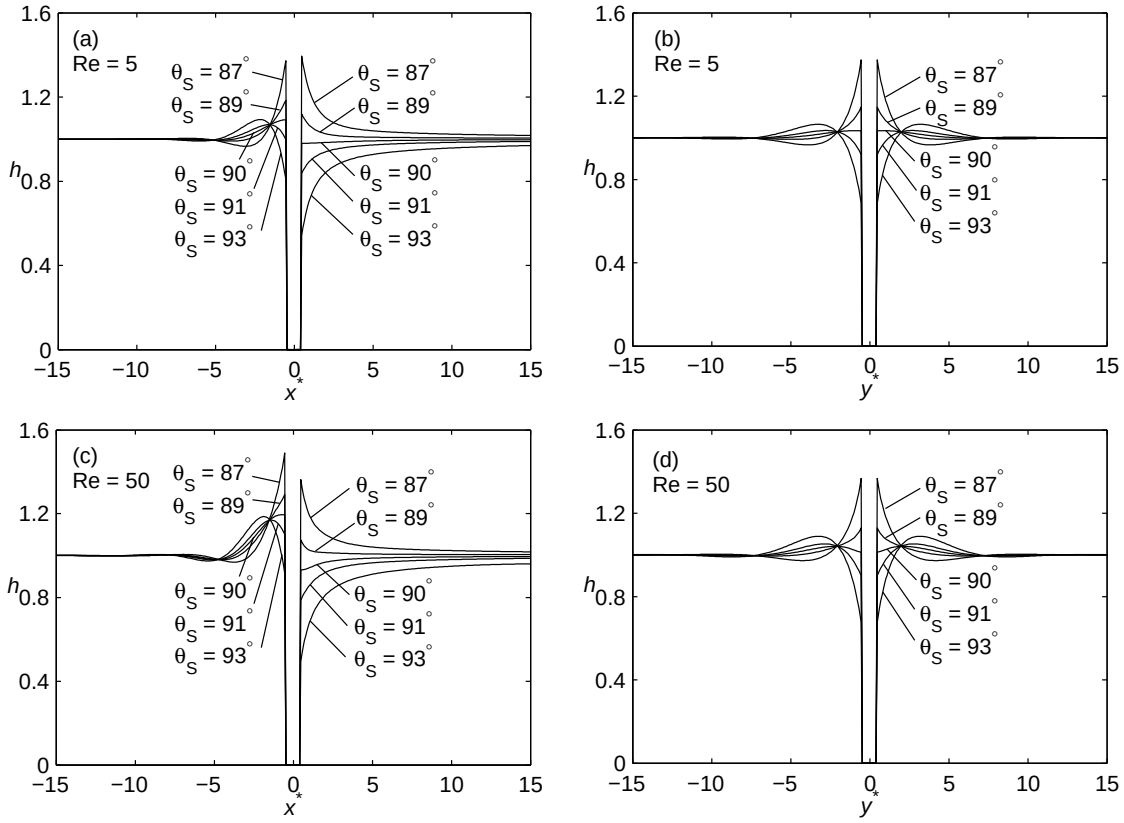

Figure 3: Effect of contact angle, θ_S, and Reynolds number, Re, on (left) streamwise and (right) spanwise centre-line free-surface profiles through the centre of a square occlusion for Re= 5 (top) and Re= 50 (bottom).

Figure 4 shows the effect of inertia and aspect ratio on the three-dimensional free-surface disturbance that results from flow past a rectangular occlusion. It clearly demonstrates how increasing Re from 5 to 50 leads to typically a doubling of the free-surface disturbance upstream of the occlusion and a strengthening of the bow wave shed from the sides of the occlusion. Increasing aspect ratio also has a dramatic effect on the free-surface disturbances, most noticeably on the increased magnitude of the upstream free-surface disturbances. In fact this is to be expected since, in the limit $A \to \infty$, the fluid film would have to climb over the occlusion in order to satisfy mass continuity.

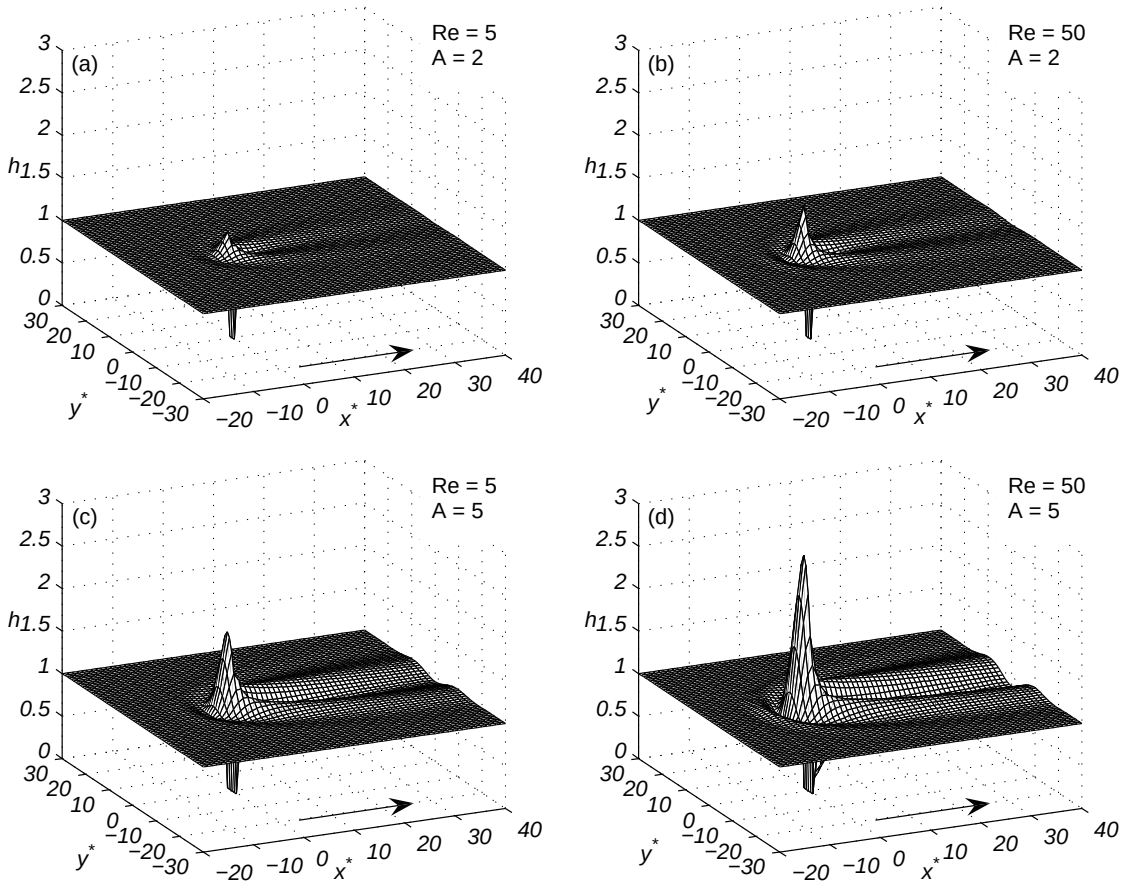

Figure 4: Free-surface plot for flow over a two-dimensional localised rectangular occlusion with $\theta_S = \frac{\pi}{2}$ showing the effect of Reynolds number, Re, and aspect ratio, A, on the free surface disturbance.

Finally, the magnitude of these free-surface disturbances are shown more clearly by the corresponding streamwise and spanwise free-surface profiles shown in Figures 5(a) and 5(b) respectively. Figure 5(a) shows that increasing Re from 5 to 50 leads to an increase in the film thickness at the upstream occlusion boundary from 1.30 to 1.61 and 1.98 to 2.92 for occlusions with $A = 2$ and $A = 5$ respectively. It also shows the effect of Re and A on the degree of film thinning near the downstream occlusion boundary. For $A = 2$, increasing Re from 5 to 50 leads to a reduction in film thickness at the downstream occlusion boundary from 0.89 to 0.76. For $A = 5$, the localised thinning is much more pronounced with the film thickness reducing from 0.42 for Re = 5 to only 0.13 for Re = 50, suggesting that the substrate may become effectively dry just downstream of the occlusion for larger Re values. Such localised film thinning is very important in, for example, cooling applications since they can have a major influence on the achievable heat transfer rates into cooling films[2].

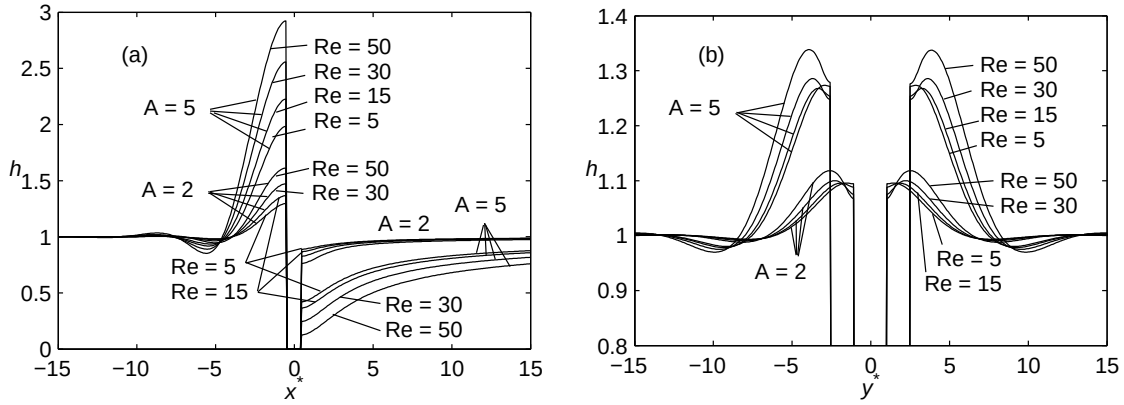

Figure 5: Effect of Re and A on (a) streamwise and (b) spanwise centre-line free-surface profiles through the centre of a rectangular occlusion.

5 CONCLUSIONS

In addition to its well-known influence on free-surface stability, this paper has shown how both inertia and occlusion geometry can enhance free-surface disturbances that result from thin film flow past occlusions. Generally, increasing inertia leads to localised film thickening near the upstream occlusion boundary and film thinning near the downstream boundary. Each of these features is amplified by increasing the occlusion aspect ratio. Static contact angle θ_S also has a significant influence on film thicknesses near the occlusion and increasing θ_S tends to reduce film thicknesses upstream and increase film thicknesses downstream of the occlusion. Detailed knowledge of such film thickness variations is essential for optimal design in practical applications.

6 ACKNOWLEDGEMENT

S. Veremieiev gratefully acknowledges the financial support of the European Union Marie Curie Action, contract MEST-CT-2005-020599.

REFERENCES

[1] S.J. Abbott and P.H. Gaskell, Mass production of bio- inspired structured surfaces, Proc. IMechE, Part C: J. Mech. Eng. Sci., 221(2007) 1181-1191.

[2] S.J. Baxter, H. Power, K.A. Cliffe and S. Hibberd, Three-dimensional thin film flow over and around an obstacle on an inclined plane, Phys. Fluids, 21(3)(2009) 032102-032102-23,.

[3] K. Helbig, R. Nasarek, T. Gambaryan-Roisman and P. Stephan, Effect of longitudinal minigrooves on flow stability and wave characteristics of falling liquid films, J. Heat Transfer, 131(1)(2009) 011601-011608,

[4] N.C. Linn, C.-H. Sun, P. Jiang and B. Jiang, Self-assembled biomimetic antireflection coatings, Appl. Phys. Lett., 91(2007) 101108.

[5] H.C. Ko, M.P. Stoykovich, J. Song, V. Malyarchuk, W.M. Choi, C.-J. Yu, J.B. Geddes, J. Xiao, Y. Huang and J.A.A. Rogers, A hemispherical electronic eye camera based on compressible silicon optoelectronics, Nature, 454(2008) 748-753.

[6] M.M.J. D*écré* and J.C. Baret, Gravity-driven flows of viscous liquids over two-dimensional topographies., J. Fluid Mech., 487(2003), 147-166.

[7] C.R. Glass, K.F.A. Walters, P.H. Gaskell, Y.C. Lee, H.M. Thompson, D.R. Emerson and X-J Gu, Recent advances in computational fluid dynamics relevant to the modelling of pesticide flow on leaf surfaces, Pest Manag. Sci., 66 (2010), 2-9.

[8] M. Sellier, Y.C. Lee, H.M. Thompson and P.H. Gaskell, Thin film flow on surfaces containing arbitrary occlusions, Computers & Fluids, 38(2009), 171-182.

[9] S.J. Baxter, H. Power, K.A. Cliffe and S. Hibberd, Free surface Stokes flows obstructed by multiple obstacles, Int. J. Num. Meth. Fluids, 62 (2010), 530-564.

[10] S. Veremieiev, H.M. Thompson, Y.C. Lee, and P.H. Gaskell, Inertial thin film flow on planar surfaces featuring topography. Comp. & Fluids, 39(3)(2010), 431-450.

[11] R.V. Craster and O.K. Matar, Dynamics and stability of thin liquid films, Rev. Mod. Phys., 81(3)(2009), 1131-1198.

[12] T.J. Chung, Computational Fluid Dynamics., Cambridge University Press: Cambridge (2002).